Journal of Inflammation Research

Dovepress
Taylor & Francis Group

Open Access Full Text Article

ORIGINAL RESEARCH

Comprehensive Analysis of Differences in N6-Methyladenosine RNA Methylation Groups in CVB3-Induced Viral Myocarditis and Identification of the Anti-Apoptotic Role of RBM15B

Yanan Hu[1,2,*], Jiahui Lin[3,*], Lu Yi[4], Sha Cheng[5], Gao You[6], Huan Chang[7], Hanmin Liu[1,2], Zuocheng Yang[8], Shuyue Chen[9]

[1]Department of Pediatric Pulmonology and Immunology, West China Second University Hospital, Sichuan University, Chengdu, 610041, People's Republic of China; [2]Key Laboratory of Birth Defects and Related Diseases of Women and Children (Sichuan University), Ministry of Education, Chengdu, 610041, People's Republic of China; [3]Department of Gastroenterology, The Seventh Affiliated Hospital, Sun Yat-Sen University, Shenzhen, 518107, People's Republic of China; [4]Department of Hengyang Medical School, The First Affiliated Hospital, University of South China, Hengyang, Hunan, 421001, People's Republic of China; [5]Department of Gastroenterology, The Third Xiangya Hospital, Central South University, Changsha, Hunan, 410013, People's Republic of China; [6]Cardiovascular Surgeon Department, Intensive Care Unit, Xiangya Hospital, Central South University, Changsha, Hunan, 410013, People's Republic of China; [7]Department of Anesthesiology, The Third Xiangya Hospital, Central South University, Changsha, Hunan, 410013, People's Republic of China; [8]Department of Pediatrics, The Third Xiangya Hospital, Central South University, Changsha, Hunan, 410013, People's Republic of China; [9]Department of Plastic Surgery, The Third Xiangya Hospital, Central South University, Changsha, Hunan, 410013, People's Republic of China

*These authors contributed equally to this work

Correspondence: Zuocheng Yang; Shuyue Chen, Email yang_zcr@126.com; duiyu07@163.com

Background: Viral myocarditis (VMC) is a leading cause of sudden cardiac death in children and young adults, with Coxsackievirus B3 (CVB3) identified as the primary viral pathogen responsible. N^6-methyladenosine (m^6A), the most abundant and reversible RNA methylation modification in mammals, plays a pivotal role in regulating numerous biological processes. However, the potential effects of CVB3 infection on m^6A methylation within the myocardium remain unexplored. In this study, we investigated alterations in global RNA m^6A methylation levels during CVB3 infection using both in vitro and in vivo models, and further examined the regulatory role of the m^6A methyltransferase RBM15B in vitro.

Methods: First, the total quantity of m6A was quantified in Balb/c mice and HL-1 cells with CVB3 infection via m^6A dot blot analysis. Subsequently, m^6A methylation sequencing (MeRIP-seq) and RNA sequencing (RNA-seq) were performed on cell model, while RNA-seq was conducted on animal tissues. We further analyzed the expression of m^6A regulatory genes and their involvement in key pathways linked to VMC pathogenesis to elucidate underlying mechanisms. Given the pronounced expression of RBM15B in vitro, we knocked down RBM15B and assessed its regulatory effects on CVB3-infected HL-1 cells using Western blotting, viral plaque assays, and Calcein AM/PI double staining.

Results: Quantitative m^6A analysis revealed elevated m^6A modification levels in CVB3 infection group. MeRIP-seq identified 327 significantly altered m^6A peaks (116 upregulated, 211 downregulated). RNA-seq detected 1,597 upregulated and 2,942 downregulated mRNAs. Integrated analysis of MeRIP-seq and RNA-seq identified 38 hypermethylated-upregulated, 23 hypermethylated-downregulated, 65 hypomethylated-downregulated, and 13 hypomethylated-upregulated genes. GO and KEGG pathway analyses of these differentially methylated genes highlighted their roles in broad biological functions. Furthermore, qRT-PCR validation of mice RNA-seq data confirmed significant differences in four key genes (*Igtp, ApoI9b, Ddit3*, and *Irgm3*), along with altered expression of m^6A regulators (*IGF2BP2, EIF3H, RBM15B*, and *YTHDC2*), with *RBM15B* showing the most pronounced changes. RBM15B knockdown in HL-1 cells reduced CVB3 replication (viral plaque assay) and attenuated apoptosis induced by CVB3 infection (Calcein AM/PI staining and Western blotting).

Conclusion: These findings establish a foundation for exploring the role of m^6A methylation in CVB3-associated VMC and may provide novel therapeutic insights for managing CVB3-induced viral myocarditis.

Received: 6 December 2024
Accepted: 31 May 2025
Published: 17 June 2025

Keywords: viral myocarditis, coxsackievirus B3, m^6A, RBM15B, HL-1 cell, apoptosis

Introduction

Viral myocarditis (VMC) is a myocardial inflammatory disorder triggered by infection with cardiotropic viruses, often resulting in acute or chronic cardiac damage.[1–3] This condition arises primarily from adverse immune responses to viral infection, accompanied by myocardial injury, reparative fibrosis, and progression to heart failure during viral clearance. Among the various viral pathogens implicated, Coxsackievirus B3 (CVB3), a positive-sense single-stranded RNA virus, is the most frequently identified causative agent.[4,5] Despite extensive research efforts, effective antiviral therapies for VMC are still unavailable. This underscores the critical need for deeper investigation into the molecular mechanisms underlying CVB3-induced myocardial damage, which could pave the way for novel therapeutic approaches.

Recent studies emphasize the role of epigenetic regulation in inflammation, particularly through RNA methylation modifications. N^6-Methyladenosine (m^6A), the most common post-transcriptional modification in eukaryotic RNA, is regulated by "writers", "erasers", and "readers".[6–9] Methyltransferases like METTL3, METTL14, and WTAP act as "writers" to add methyl groups, while demethylases such as ALKBH5 and FTO serve as "erasers" to remove them. "Readers", including YTH domain proteins (eg, YTHDC1, YTHDF2), recognize m^6A sites to influence RNA processing.[10] m^6A regulates key mRNA processes such as splicing, stability, and translation, playing a vital role in mRNA fate.[11–15] m^6A modifications have been linked to inflammatory diseases like pulmonary inflammation, colitis, and coronary artery disease,[16–18] as well as to viral RNA regulation in HIV, Zika virus, and SARS-CoV-2.[19–22] However, the function and regulatory landscape of m6A modifications in CVB3-induced VMC remain largely unexplored, representing a major knowledge gap in the field.

In this research, high-throughput MeRIP-seq was utilized to map m^6A modifications in HL-1 cardiomyocytes infected with CVB3. Analyses of differentially methylated genes (DMGs), differentially expressed genes (DEGs), and differentially methylated and expressed genes (DMEGs) were conducted, with gene ontology (GO) and Kyoto Encyclopedia of Genes and Genomes (KEGG) enrichment highlighting their functional significance. Furthermore, mouse mRNA Sequencing (RNA-Seq) data was employed to confirm the expression patterns of m^6A-regulated genes and critical targets through qRT-PCR, revealing consistency across in vitro and in vivo models. Building upon these analytical findings, we hypothesize that m^6A modifications contribute to CVB3-induced myocardial damage, with RBM15B playing a regulatory role in apoptosis, and subsequently conducted systematic experimental validations. Altogether, our findings provide the first comprehensive characterization of m^6A epitranscriptomic alterations during CVB3 infection, highlighting the central role of m^6A methylation in mediating viral myocarditis. This work offers new molecular insights into VMC progression and suggests potential therapeutic avenues targeting RNA methylation machinery.

Materials and Methods

Cell Culture

HeLa cells (obtained from the Institute of Cancer Research, Central South University, China) were grown in DMEM (Gibco, CA, USA) supplemented with 10% FBS (Biological Industries, Israel) and antibiotics (100 U/mL penicillin and 100 μg/mL streptomycin; Life Technologies, NY, USA). HL-1 cells (Merck, Darmstadt, Germany) were cultured in Claycomb medium (Sigma-Aldrich, MO, USA), enriched with 10% FBS, 1% antibiotics, 0.1 mm norepinephrine, and 2 mm glutamine (all from Sigma-Aldrich). All cells were cultured in a humidified incubator set at 37°C with 5% CO_2.

Virus and Infection

The CVB3 Nancy strain (obtained from Shanghai Jiaotong University School of Medicine, China) was amplified in HeLa cells and preserved at −80°C. Viral titers were determined using plaque assays. For infection experiments, HL-1 cells were seeded in 6-well plates one day prior and serum-starved overnight in medium containing 2% FBS. Then infect the cells with CVB3 (MOI=10, based on the optimal infection conditions established through prior studies). Following a 1-hour incubation, the cells were washed with PBS and maintained in fresh 2% FBS medium for an additional

48 hours. Control cells (Sham group) were exposed to 2% FBS medium without viral infection. Supernatants were collected post-culture and preserved at −80°C for later plaque assay analysis.

Animal Models

Male BALB/c mice (4 weeks old, 18–20 g, SPF-grade) were purchased from the Laboratory Animal Center of Central South University and housed under SPF conditions. Following a 1-week acclimation period, all mice were divided into different groups based on complete randomization. The CVB3 group received intraperitoneal injection of CVB3 as reported in literature[23] (10^3 $TCID_{50}$, diluted in PBS), while Sham group received an equal volume of saline. Mice were observed daily for changes in appearance, behavior, and survival status. On day 7 post-infection, they were euthanized via cervical dislocation, and collected blood samples and cardiac tissues. Mice that either succumbed during the experiment or showed no evidence of myocardial inflammatory cell infiltration in the CVB3 group were excluded from the study. All procedures involving animals were approved by the Central South University Animal Experimentation Management Committee (Approval No. 2021sydw0104) and adhered to ethical standards to minimize animal suffering.

Hematoxylin and Eosin (HE) Staining

The heart tissues were preserved in 4% paraformaldehyde, embedded in paraffin, and cut into 5 μm sections. These sections underwent deparaffinization in xylene, rehydration through a graded series of ethanol, and staining with HE. Finally, the stained sections were mounted with neutral balsam and examined using an optical microscope.

ELISA Assay

The levels of CK-MB and cTnT were conducted using ELISA kits provided by JINGMEI Biotechnology (Jiangsu, China). The assays were conducted following the manufacturer's protocol, and absorbance measurements were obtained using a Multilabel Plate Reader (PerkinElmer, MA, USA).

Immunofluorescence (IF) Assay

Paraffin-embedded tissue sections underwent dewaxing, rehydration, and antigen retrieval, followed by overnight incubation at 4°C with primary antibody targeting CVB3 (1:100). Cells were fixed in 4% paraformaldehyde, then treated with 0.5% Triton X-100 for permeabilization and incubated with 5% goat serum for blocking (2 hours). Primary antibodies against FOXO1 (1:100) were applied and incubated overnight at 4°C. Subsequently, Secondary antibodies conjugated to Alexa Fluor 594 or 488 (1:200) were applied for 1 hour, followed by DAPI staining (125 μg/mL) for 15 minutes. Visualization was carried out using a Zeiss fluorescence microscope (Jena, Germany). The antibodies in this study are provided in Supplementary Table S2.

Viral Plaque Assay

Culture media underwent serial dilutions and were applied to HeLa cells plated in six-well dishes, each well containing 1×10^6 cells. After an hour of incubation, cells were washed by PBS and overlaid with 2% soft agar. The cultures were then incubated for 72 hours. Viral plaques were visualized using the VisionWorks system (Analytik Jena AG, Jena, Germany), and the titers were quantified in PFU/mL.

Cell Proliferation and Cytotoxicity Assay

Cell proliferation and cytotoxicity were assessed with the Calcein AM/PI Double Stain Kit (MKBio, Shanghai, China). HL-1 cells were incubated with Calcein-AM (2 μM) and PI (4.5 μM) at 37°C for 10 minutes. Fluorescence imaging was performed and recorded using a Zeiss fluorescence microscope.

RNA Extraction and Quantitative Real-Time PCR (RT-PCR)

Total RNA was extracted with TRIzol reagent (Invitrogen) and quantified using the NanoDrop 2000 (Thermo Scientific, MA, USA). cDNA was synthesized with HiScript III RT SuperMix (Vazyme, Nanjing, China). qRT-PCR was conducted

on a LightCycler 480II system (Roche, Basel, Switzerland), with β-actin as the normalization control. Primer sequences are provided in Supplementary Table S1.

Western Blotting

Myocardial tissues and cells were lysed in RIPA buffer (Beyotime, Shanghai, China) supplemented with protease and phosphatase inhibitors (Roche). The homogenates were separated by SDS-PAGE (8–12%) and transferred onto PVDF membranes (Millipore, CA, USA). Membranes were first blocked with 5% non-fat milk, then incubated overnight at 4°C with primary antibodies, and subsequently exposed to secondary antibodies at room temperature for 1 hour. Protein bands were visualized utilizing an ECL detection kit (Biosharp, Anhui, China), and the bands were subsequently analyzed with the VisionWorks imaging system. Antibodies are detailed in Supplementary Table S2.

m^{6}A Dot Blot Analysis

A total of 1 μg of RNA was denatured at 65°C for 10 minutes, then cooled on ice before being transferred onto nylon membranes. After UV cross-linking for 10 minutes and blocking with 5% non-fat milk, the membranes underwent overnight incubation at 4°C with the m^{6}A antibody (1:600, HA601049). Afterward, a secondary antibody conjugated with HRP (1:2000) was applied for 1 hour. Protein bands were then detected using a chemiluminescence imaging system. Equal loading was confirmed by staining membranes with 0.02% methylene blue for 30 minutes, followed by rinsing and photographing.

RNA-Seq and m^{6}A-RNA Immunoprecipitation Sequencing (m^{6}A-Seq)

Total RNA from mouse heart tissue and HL-1 cells was extracted using TRIzol. Poly(A) RNA was extracted from 50 μg of total RNA through two rounds of purification using Dynabeads Oligo(dT) (Thermo Fisher). The quality of the RNA was assessed using a Bioanalyzer 2100 (Agilent), and ribosomal RNA was eliminated through the use of the Epicentre Ribo-Zero Gold Kit (Illumina). Fragmented RNA underwent m^{6}A immunoprecipitation with Dynabeads and an m^{6}A antibody (Synaptic Systems, Germany), followed by cDNA synthesis for sequencing.

Bioinformatics Analysis

Raw data quality was assessed using Fastp (https://github.com/OpenGene/fastp) and aligned to the Mus musculus genome with HISAT2 (http://daehwankimlab.github.io/hisat2). Differential peak analysis was performed using exomePeak (https://bioconductor.org/packages/release/bioc/html/exomePeak.html), and annotations were completed with ANNOVAR (http://www.openbioinformatics.org/annovar/). Motif analysis utilized MEME2 (http://meme-suite.org) and HOMER (http://homer.ucsd.edu/homer/motif). Gene expression was quantified with StringTie (https://ccb.jhu.edu/software/stringtie), and differential expression was analyzed using edgeR (https://bioconductor.org/packages/edgeR) with thresholds of fold change (FC) ≥ 2 or ≤ 0.5 and p-value < 0.05.

Statistical Analysis

All experiments were conducted in triplicate to ensure consistency, and the data are presented as mean ± standard deviation (S.D). Statistical analyses were performed using SPSS software (IBM SPSS 26.0). Two-tailed independent t-tests were employed for comparisons between two groups with normally distributed data. For comparisons between multiple groups, one-way ANOVA with Tukey's post hoc test was applied. For non-normally distributed data, the Mann–Whitney *U*-test was used. Statistical significance was defined as $p < 0.05$.

Results

Increased m^{6}A Levels in CVB3-Induced Viral Myocarditis

To explore the mechanisms underlying CVB3-induced viral myocarditis, a mouse model was established via intraperitoneal injection of 10^3 $TCID_{50}$ CVB3. CVB3-infected mice exhibited significant weight loss, smaller heart sizes, and irregular myocardial surfaces (Figure 1A and B). Serum CK-MB and cTnT levels were markedly higher compared to

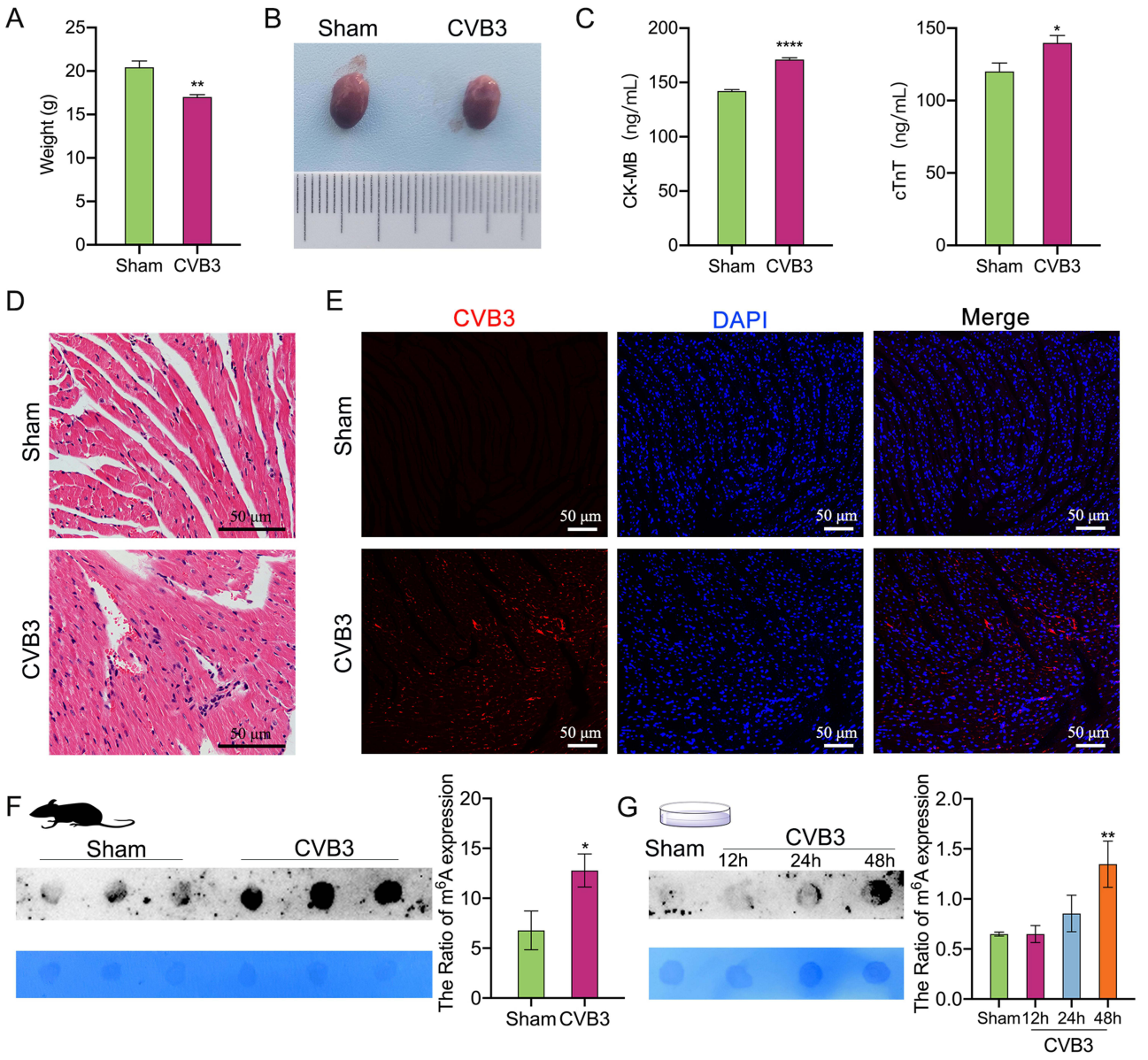

Figure 1 Establishment of CVB3 infection model and determination of total m^{6}A. (**A**) Body weights of Sham and CVB3 groups; n = 6. (**B**) General morphology of the hearts of Sham and CVB3 groups. (**C**) Comparison of serum myocarditis inflammatory markers CK-MB and cTnT between Sham and CVB3 groups; n = 6. (**D**) Representative images of HE staining of mouse myocardium from Sham and CVB3 groups (scale bar = 50 μm); n = 6. (**E**) IF staining of CVB3 (red) in mouse myocardial tissue in the Sham and CVB3 groups, blue staining indicates DAPI nuclear staining (scale bar = 50 μm); n = 6. (**F**) m^{6}A dot blot analysis of myocardial tissues from Sham and CVB3 groups of mice; n=3. (**G**) m^{6}A dot blot analysis of Sham and CVB3 groups of HL-1 cell; n=3. *p < 0.05, **p < 0.01, ****p < 0.0001.

Sham group (Figure 1C). HE staining revealed intense inflammatory infiltration in myocardial fibers and perivascular regions (Figure 1D), while immunofluorescence confirmed substantial CVB3 presence in myocardial tissues (Figure 1E), validating the model. Notably, myocardial m^{6}A methylation levels were significantly elevated in CVB3-infected mice (Figure 1G). A similar increase was observed in HL-1 cells, with peak m^{6}A levels at 48 hours post-infection (Figure 1F). HL-1 cells infected with CVB3 (MOI = 10) for 48 hours were subsequently analyzed by sequencing.

Overview of m^{6}A RNA Immunoprecipitation Sequencing in CVB3-Infected HL-1 Cells

In the MeRIP-seq analysis, the CVB3 and Sham groups produced an average of 90,779,293 and 90,038,791 valid reads, respectively, while RNA-seq yielded averages of 89,876,025 and 91,116,208 reads (Supplementary Table S3). Valid read mapping rates were 95.04% (Sham) and 94.47% (CVB3) for immunoprecipitated (IP) samples, and 91.87% (Sham) and

https://doi.org/10.2147/JIR.S503823

87.82% (CVB3) for input samples (Supplementary Table S4). Clean reads predominantly mapped to exonic regions, accounting for 92.68% (Sham) and 93.05% (CVB3) of total reads (Figure S1). m^{6}A modifications were enriched near the transcription start site (TSS) and transcription end site (TES) (Figure 2A). Differential m^{6}A peaks were primarily located in the 3′UTR (Sham: 32.5%; CVB3: 33.5%) and coding sequence (CDS) regions (Sham: 32%; CVB3: 32.9%) (Figure 2B and C), with similar peak distributions across groups (Figure 2D). A total of 327 significant differential peaks were identified, with 116 showing upregulation and 211 showing downregulation, based on criteria of |log2(FC)| > 1 and *p*-value < 0.05 (Figure 2E). Both groups exhibited the characteristic m^{6}A motif 5′-RRACH-3′ (where R = A or G; H = A, C, or U) (Figure 2F).

Differential m^{6}A Modifications are Associated with Key Biological Pathways

GO and KEGG enrichment analyses highlighted the functional roles of m^{6}A-modified genes in CVB3-infected HL-1 cells. GO analysis showed that hypermethylated genes were primarily associated with the “membrane” in the cellular component category, while hypomethylated genes were enriched in the “nucleus” (Figure 3A and B). Both groups were

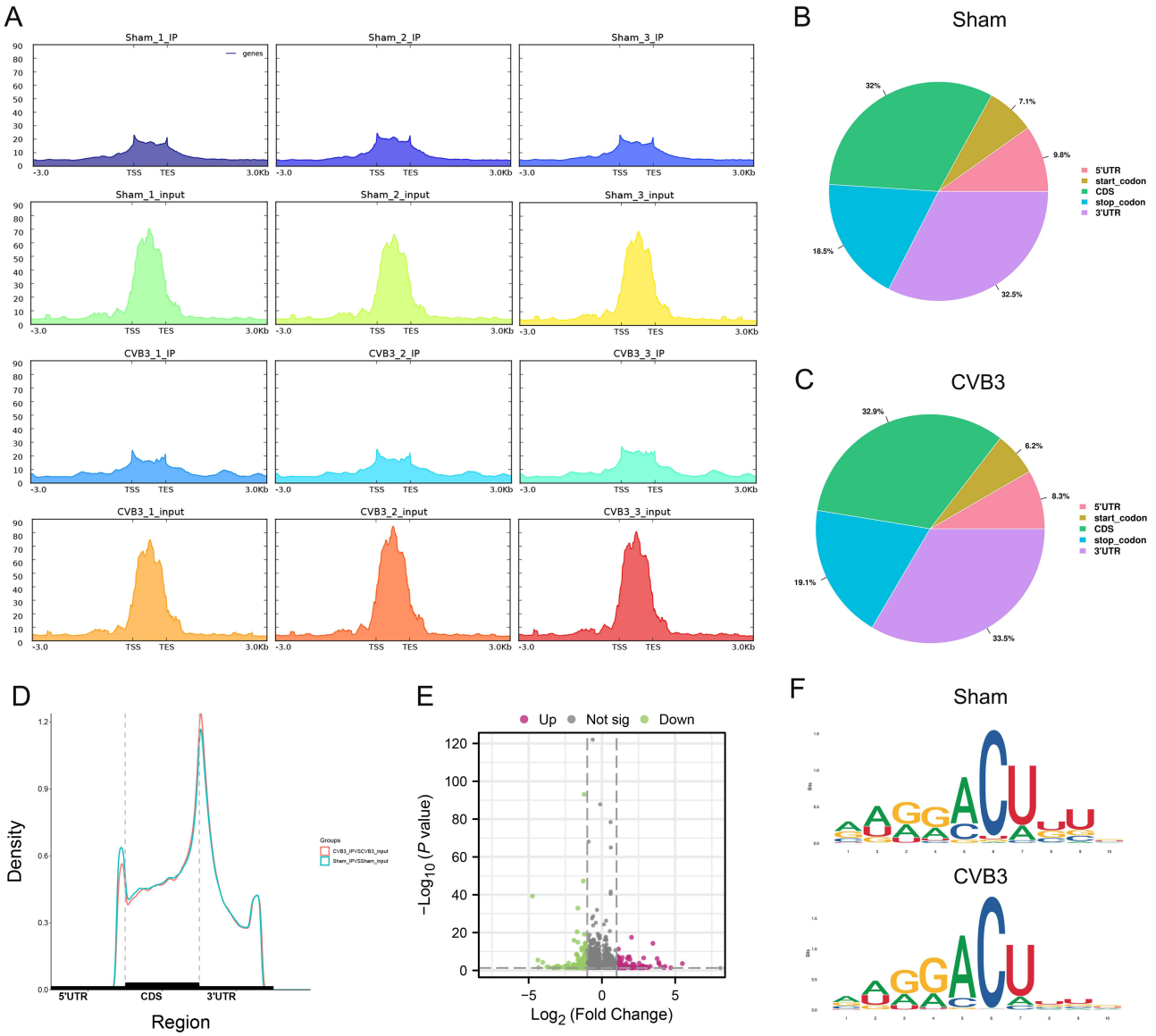

Figure 2 Significant dysregulation of m^{6}A peaks during CVB3 infection of HL-1 cells. (**A**) Enrichment of peaks near gene transcription start sites. (**B, C** and **D**) Distribution of differentially methylated m^{6}A peaks in Sham and CVB3 groups. (**E**) Volcano plot of genes with differential m^{6}A peaks (|log2(FC)|>1 and p-value < 0.05). (**F**) Motif map of m^{6}A modifications in the Sham and CVB3 groups.

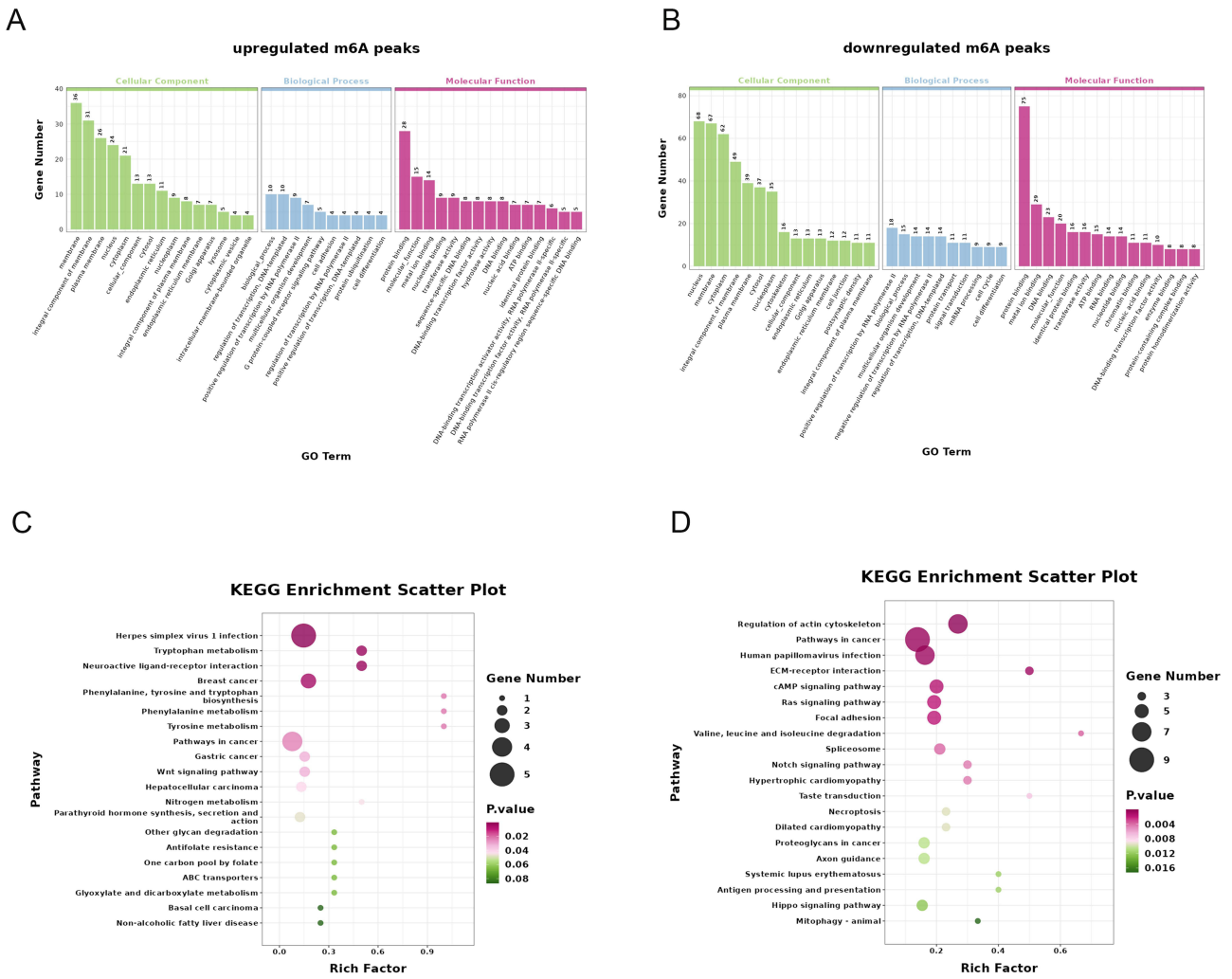

Figure 3 Differential m^{6}A modifications are involved in important biological pathways. (**A**) GO enrichment analysis of the hypermethylated peaks. (**B**) GO enrichment analysis of the hypomethylated peaks. (**C**) KEGG pathway analysis of the hypermethylated peaks. (**D**) KEGG pathway analysis of the hypomethylated peaks.

linked to biological processes such as DNA transcription regulation, RNA polymerase II activity regulation, and cellular differentiation. For molecular functions, "protein binding", "RNA binding", and "metal ion binding" were common associations for both hyper- and hypomethylated genes (Figure 3A and B). KEGG pathway analysis revealed distinct patterns: upregulated m^{6}A-modified genes were significantly enriched in pathways such as "virus infection", "tryptophan metabolism", "neuroactive ligand-receptor interaction", and "phenylalanine metabolism" (Figure 3C). Conversely, downregulated genes were predominantly associated with "Regulation of actin cytoskeleton", "cAMP signaling pathway", and "Notch signaling pathway" (Figure 3D).

RNA-Seq Differential Gene Expression Analysis

To investigate the connection between m^{6}A modifications and gene expression, RNA-seq was performed. Hierarchical clustering revealed distinct gene expression profiles between the Sham and CVB3 groups (Figure 4A). A total of 4539 DEGs were detected, comprising 1597 upregulated and 2942 downregulated genes ($|\log2(FC)| > 1$ and p-value < 0.05) (Figure 4B). GO analysis revealed that these DEGs were primarily associated with terms such as "membrane", "calcium ion binding", and "cell adhesion" (Figure 4C). Moreover, KEGG pathway analysis demonstrated significant enrichment in pathways such as "PI3K-Akt signaling", "MAPK signaling", "cytokine-cytokine receptor interaction", and "calcium signaling" (Figure 4D). These findings indicate that m^{6}A modification is closely linked to pathways essential for cellular signaling, inflammation, and viral infection processes.

https://doi.org/10.2147/JIR.S503823

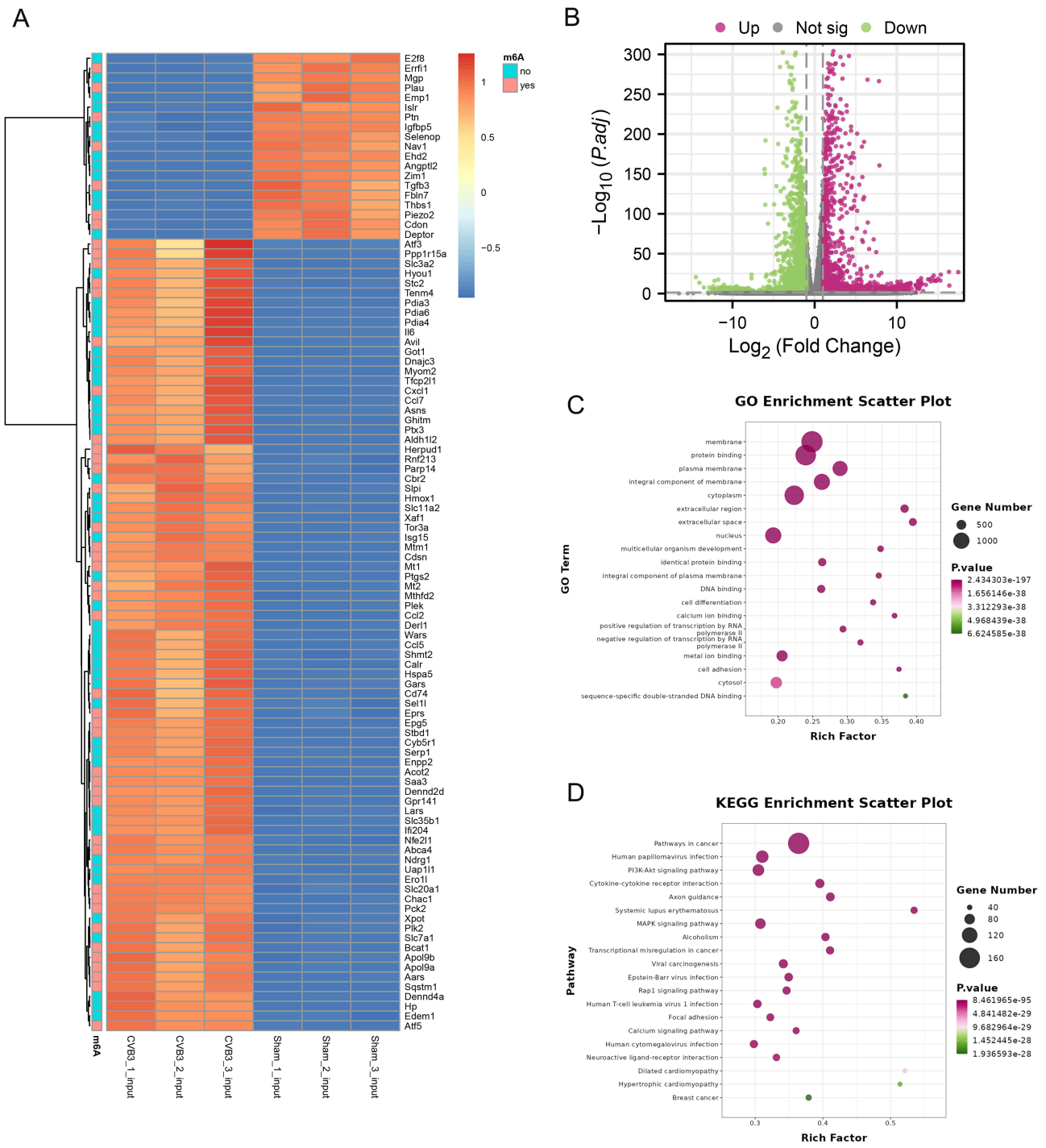

Figure 4 Differential expression gene analysis by RNA-Seq. (**A**) Heatmap showing mRNAs differentially expressed in three CVB3 group input samples and three Sham group input samples. (**B**) Volcano plot showing mRNAs differentially expressed between CVB3 and Sham groups with statistical significance (|log2(FC)| ≥1.0 and p < 0.5). (**C**) GO enrichment analysis of differential genes. (**D**) KEGG pathway analysis of differential genes.

Combined Analysis of m^{6}A-Seq and RNA-Seq

To investigate the interplay between gene expression and m^{6}A modifications, RNA-seq and m^{6}A-seq datasets were integrated. Genes were categorized based on their m^{6}A modification and expression changes: 38 genes exhibited hypermethylation with upregulation (hyper-up), 23 showed hypermethylation with downregulation (hyper-down), 65 displayed hypomethylation with downregulation (hypo-down), and 13 were hypomethylated with upregulation (hypo-up)

(Figure 5A). KEGG pathway analysis revealed the following: Hypo-up genes were significantly enriched in pathways such as "glycerophospholipid metabolism", "virus infection", "TNF signaling pathway", and "Ras signaling pathway" (Figure 5B). Hyper-down genes were associated with "complement and coagulation cascades" and "fluid shear stress and atherosclerosis" (Figure 5C). In addition, hypo-up genes were mainly enriched in "Cytokine-cytokine receptor interaction", "PI3K-Akt signaling pathway", "MAPK signaling pathway" and "FoxO signaling pathway" (Figure 5D). Hypo-

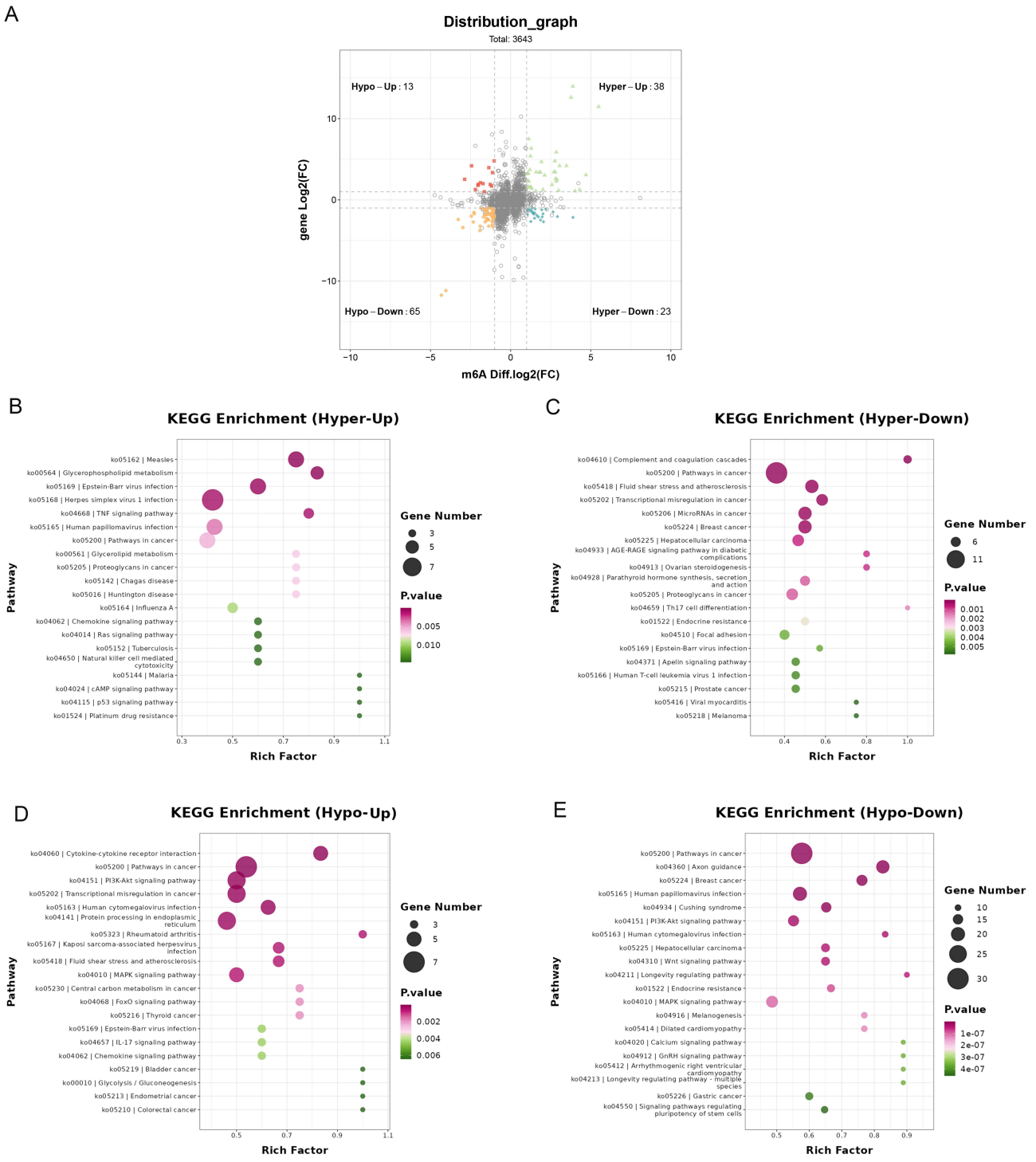

Figure 5 Combined analysis between m^{6}A-Seq and RNA-Seq. (**A**) Four-quadrant diagram of hyper-up, hyper-down, hypo-up, and hypo-down DMEG. (**B**) KEGG pathway analysis of hyper-up DMEG (**C**) KEGG pathway analysis of hyper-down DMEG. (**D**) KEGG pathway analysis of hypo-up DMEG (**E**) KEGG pathway analysis of hypo-down DMEG.

https://doi.org/10.2147/JIR.S503823

down genes were linked to pathways like "axon guidance", "Wnt signaling pathway", and "calcium signaling pathway" (Figure 5E). Additionally, Table 1 lists the top 20 transcripts exhibiting both differential m^{6}A modifications and altered mRNA expression.

Protein-Protein Interaction (PPI) Network Analysis

A PPI network was generated for the 139 DEGs linked to m^{6}A modifications using the STRING database (Figure S2A). The top 5 hub genes in the network, identified using the CytoHubba plugin in Cytoscape, were Sqstm1, Ar, Notch3, Hspa1b, and Col4a1 (Figure S2B).

Validation of Differential Genes

Comparative analysis of the in vivo and in vitro RNA-seq results revealed that 15 genes were upregulated and 1 gene downregulated in both models (Figure 6A). Genes with significant changes ($|\log2(FC)| > 2.5$ and p-value < 0.05) included *Igtp, ApoI9b, Ddit3*, and *Irgm3* (Figure 6B). qRT-PCR validation demonstrated that *ApoI9b* expression in the myocardium of the mouse model differed from the RNA-seq results, while the other genes were consistent (Figure 6C). In the HL-1 cardiomyocyte model, expression aligned with the sequencing results (Figure 6D). These findings confirm the accuracy of our sequencing data. Additionally, IGV visualization of these genes showed significant differences in m^{6}A levels (Figure 6E).

Validation of m^{6}A-Related Differential Genes

The expression levels of 36 m^{6}A regulators were evaluated using mouse RNA-seq data (Figure 7A). qRT-PCR validation of 10 common regulators in both in vivo and in vitro models revealed significant changes in the expression of *IGF2BP2, EIF3H, RBM15B*, and *YTHDC2* (Figure 7B and C). The trends observed in qRT-PCR were consistent with the RNA-seq data. Notably, *RBM15B*, which exhibited the most pronounced change in expression, was further validated by protein analysis. Consistent with qRT-PCR results, CVB3 infection led to increased *RBM15B* expression both in vivo (Figure 7D and E) and in vitro (Figure 7F and G).

Table 1 Top 20 Transcripts of Differential m6A Modification and mRNA Expression Between Sham Group and CVB3 Group

Gene Name	Change	Seq-names	m6A Modification Change						m6A Expression Change	
			Break Start	Break End	Width	Peak Region	LogFC	*p*-Value	logFC	*p*-Value
Mettl7b	Hyper-up	Chr10	128,958,273	128,958,754	482	Stop_codon	3.77	5.50E-07	12.62	9.31E-13
4930438A08Rik	Hyper-up	Chr11	58,293,571	58,294,289	719	Stop_codon	1.13	3.63E-02	7.49	5.02E-54
Slc2a6	Hyper-up	Chr2	27021362	27,021,928	567	Stop_codon	1.29	6.76E-04	6.35	0.00E+00
Gbx1	Hyper-up	Chr5	24503954	24,504,704	751	Stop_codon	2.85	2.57E-07	5.87	3.89E-05
Cd74	Hyper-up	Chr18	60,812,411	60,812,652	242	3'UTR	1.24	1.15E-02	5.39	0.00E+00
Mmp16	Hyper-down	Chr4	18116595	18,116,866	272	3'UTR	2.05	3.02E-02	−2.70	8.66E-17
Epha4	Hyper-down	Chr1	77369669	77,373,836	4168	3'UTR	1.26	3.63E-02	−2.66	1.50E-21
Sh3rf3	Hyper-down	Chr10	58,813,388	58,813,868	481	Start_codon	1.87	1.95E-02	−2.48	2.63E-28
Rnasel	Hyper-down	Chr1	153753711	153,754,011	301	Start_codon	1.49	3.72E-02	−2.26	1.10E-26
Dnajc22	Hyper-down	Chr15	99,101,749	99,104,677	2929	Stop_codon	3.89	2.00E-04	−2.16	3.03E-05
Daam2	Hypo-down	Chr17	49,458,388	49,458,659	272	Stop_codon	−4.32	2.69E-02	−11.73	4.26E-19
Ppl	Hypo-down	Chr16	5,086,650	5,087,010	361	3'UTR	−1.92	6.61E-04	−3.77	5.17E-22
Lrrtm2	Hypo-down	Chr18	35,213,825	35,213,916	92	Exonic	−2.98	6.03E-03	−3.41	1.82E-10
Pxylp1	Hypo-down	Chr9	96824594	96,825,375	782	Stop_codon	−1.13	5.37E-08	−3.28	2.19E-115
Gper1	Hypo-down	Chr5	139426785	139,427,800	1016	Stop_codon	−1.90	1.26E-16	−3.22	8.91E-56
Angptl6	Hypo-up	Chr9	20873807	20,874,017	211	Stop_codon	−1.03	3.16E-05	4.80	5.55E-173
Cdsn	Hypo-up	Chr17	35,555,424	35,555,723	300	Exonic	−1.36	2.51E-11	3.97	0.00E+00
Slc6a9	Hypo-up	Chr4	117869085	117,874,191	5107	3'UTR	−1.13	5.01E-10	3.37	0.00E+00
Ptger2	Hypo-up	Chr14	44,988,880	44,989,120	241	Start_codon	−1.72	8.71E-03	2.00	2.17E-19
Sqstm1	Hypo-up	Chr11	50,199,635	50,200,175	541	3'UTR	−1.27	5.01E-48	1.91	0.00E+00

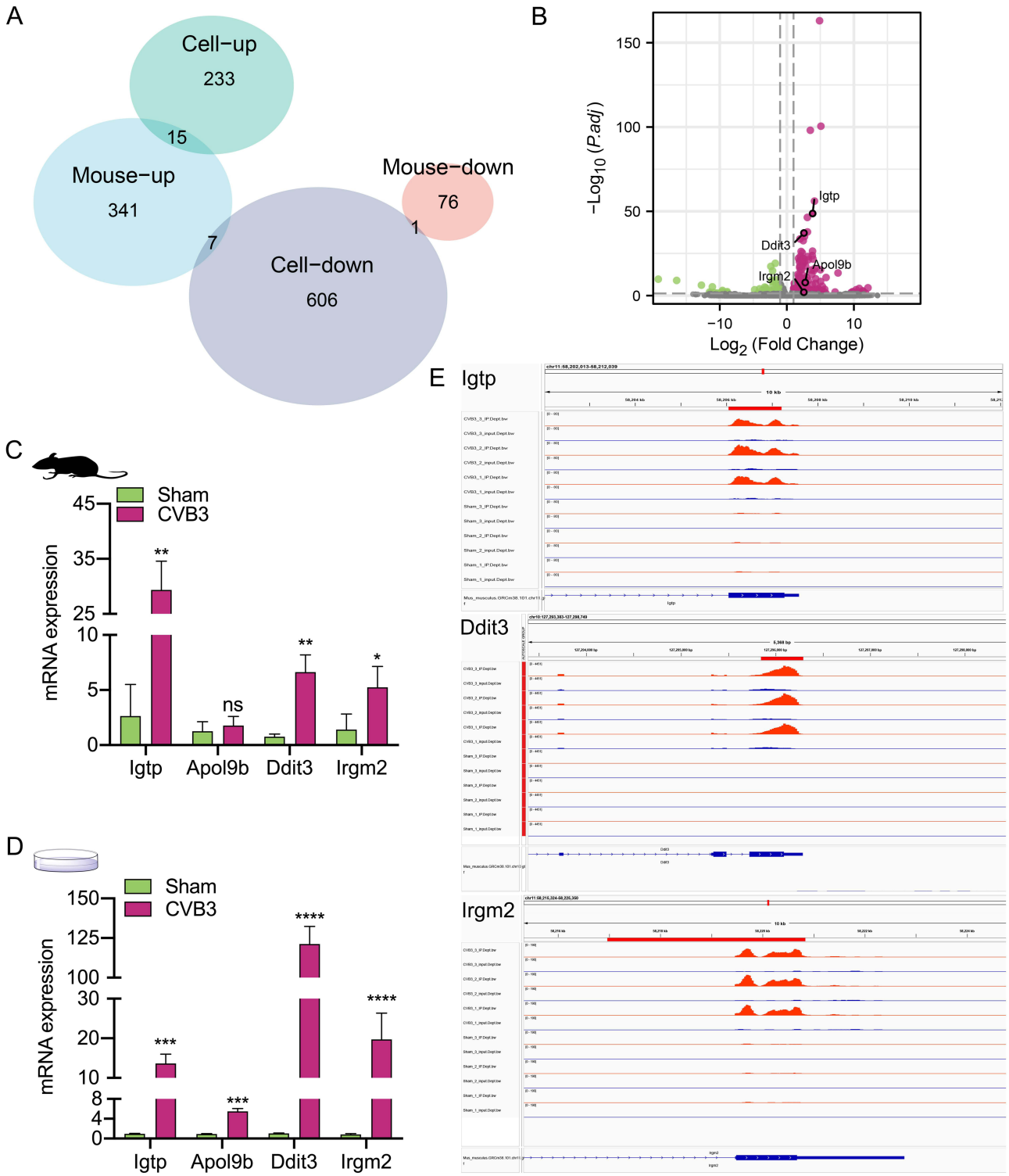

Figure 6 Validation of differentially expressed genes. (**A**) Wayne plots of in vivo and in vitro RNA-seq sequencing results. (**B**) Volcano plot showing mRNAs that were differentially expressed simultaneously after comparison of in vivo and in vitro RNA-seq sequencing results with statistical significance (|log2(FC)| ≥ 1.0 and *p*-value < 0.5). (**C** and **D**) In vivo and in vitro validation of differentially expressed genes. (**E**) IGV visualization showing three key m^{6}A-modified genes. *p < 0.05, **p < 0.01, ***p < 0.001, ****p < 0.0001.
Abbreviation: ns, no statistical significance.

Knockdown of RBM15B Ameliorates CVB3 Infection in HL-1 Cardiomyocytes

To explore the function of RBM15B during CVB3 infection, HL-1 cells were transfected with si-RBM15B or a non-targeting control siRNA (si-NC) prior to infection with CVB3. Plaque assays revealed a significant reduction in viral

https://doi.org/10.2147/JIR.S503823

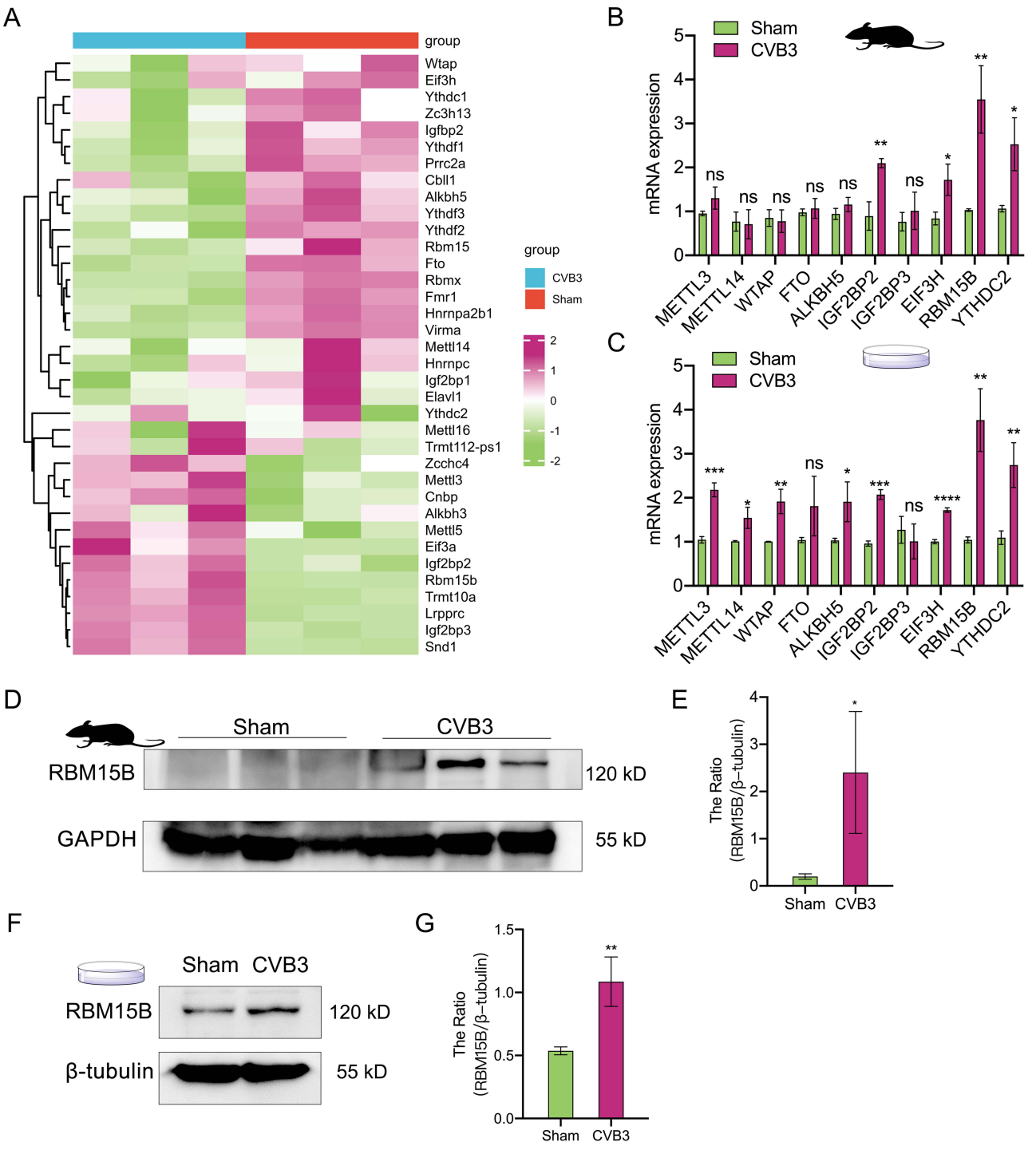

Figure 7 Validation of m^{6}A-associated differentially expressed genes (**A**) Heatmap of m^{6}A regulators in sequenced mouse samples. (**B** and **C**) qRT- PCR results of 10 common m^{6}A regulators in vivo and in vitro. (**D** and **E**) Analysis of RBM15B protein levels in mouse samples from Sham and CVB3 groups by Western blotting. (**F** and **G**) Analysis of RBM15B protein levels in HL-1 cell samples from Sham and CVB3 groups by Western blotting. *p < 0.05, **p < 0.01, ***p < 0.001, ****p < 0.0001.
Abbreviation: ns, no statistical significance.

replication in the si-RBM15B group compared to the si-NC group (Figure 8D). Calcein AM/PI double staining showed decreased cytotoxicity in the si-RBM15B group (Figure 8E). Analysis of apoptotic proteins showed that RBM15B knockdown led to a significantly reduced Bax/Bcl-2 ratio and lower Cleaved-Caspase3 levels compared to the control (Figure 8A–C). These findings indicate that silencing RBM15B mitigates CVB3-induced apoptosis in HL-1 cardiomyocytes.

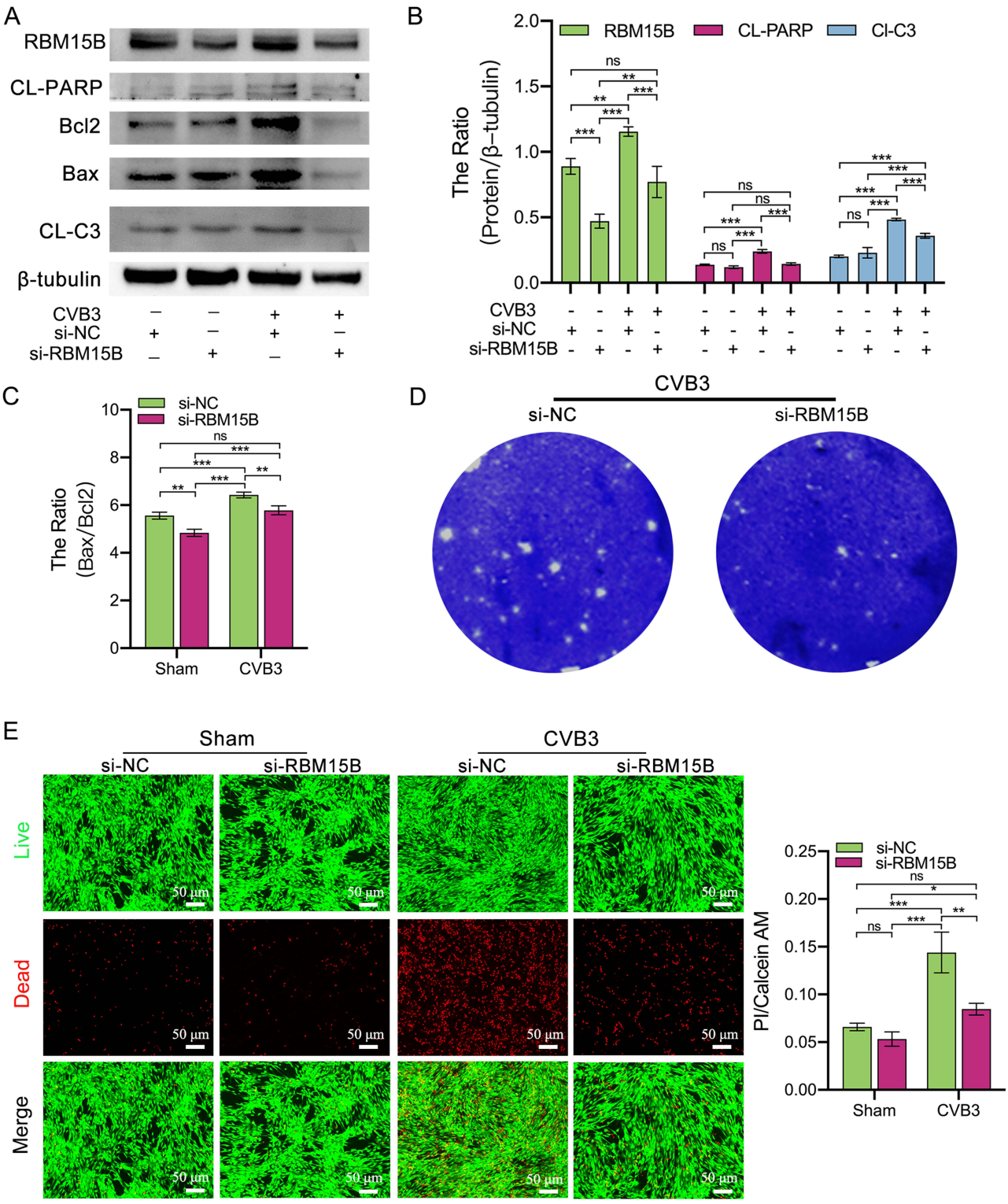

Figure 8 Knockdown of RBM15B ameliorates HL-1 cell apoptosis caused by CVB3 infection. (**A**–**C**) After transfection of HL-1 cells with si-RBM15B or si-NC, the cells were harvested under the same infection conditions and analyzed by Western blotting to determine the expression of RBM15B, cleaved-PARP, Bax/Bcl2, and cleaved-caspase3; n = 3. (**D**) Cultures from the si-NC group and si- RBM15B group were collected 48 h after infection with CVB3, respectively, and viral plaque assay was performed using Hela cells; n = 3. (**E**) Calcein AM/PI double staining assay was used to assess the cytotoxicity of HL-1 cells after transfection with si-NC and si-RBM15B at CVB3 infection (48 h) (scale bar = 50 μm). *p < 0.05, **p < 0.01, ***p < 0.001, ****p < 0.0001.

Abbreviation: ns, no statistical significance.

https://doi.org/10.2147/JIR.S503823

Discussion

CVB3, belonging to the enterovirus genus and characterized by a positive-sense RNA genome, is the primary pathogen responsible for VMC.[24] VMC is characterized by viral-induced myocardial injury followed by a persistent inflammatory response.[24] Previous studies have suggested that acute myocarditis induced by CVB3 results from direct viral damage to myocardial cells, which is subsequently followed by inflammation.[25] m^6A, a reversible RNA modification, plays a critical role in regulating gene expression and has been implicated in inflammatory responses associated with pulmonary inflammatory diseases, spontaneous colitis, and coronary artery disease.[16–18] Furthermore, m^6A modifications have been identified in viral RNA transcripts, including those of Rous sarcoma virus, influenza virus, simian virus 40, avian sarcoma virus, adenovirus, and coronaviruses.[22,26–28] However, the distribution, functional roles, and regulatory mechanisms of m6A in CVB3-induced viral myocarditis remain unexplored. This study focuses on elucidating the impact of m^6A modifications on the progression of CVB3-induced VMC.

We observed that CVB3 infection significantly increased m^6A methylation in both in vitro and in vivo models. MeRIP-seq analysis revealed distinct m^6A modification profiles between CVB3-infected and Sham controls, identifying 327 differentially methylated peaks—116 upregulated and 211 downregulated. These modifications were primarily enriched in the 3′ UTR and CDS regions, which aligns with previous studies linking m^6A modifications to mRNA stability, localization, and translation.[29] Notably, m^6A modifications were linked to key biological pathways.[30] Upregulated m^6A peaks were enriched in pathways associated with "viral infection", "tryptophan metabolism", and "neuroactive ligand-receptor interactions", while down-regulated peaks were involved in pathways such as "actin cytoskeleton regulation", "cAMP signaling", and "Ras signaling." These pathways are critical for viral replication, inflammation, and autophagy, all of which play pivotal roles in CVB3-induced myocarditis.[31–33] These results indicate that m^6A modifications are not randomly distributed but functionally associated with critical signaling cascades relevant to CVB3 pathogenesis.

To investigate how m^6A modifications influence CVB3 infection in HL-1 cells, we integrated m^6A methylation patterns with transcription factor motifs to uncover key signaling pathways involved. As in previous studies, pathways like PI3K-Akt, MAPK, Rap1, and calcium signaling were significantly enriched.[34–36] m^6A modifications have been shown to regulate gene expression in a context-dependent manner.[37–39] Therefore, we categorized the DMEGs into four groups: hyper-up, hyper-down, hypo-up, and hypo-down. KEGG analysis revealed that hypo-up genes were enriched in pathways related to "glycerophospholipid metabolism", "viral infection", and "TNF signaling", whereas hyper-down genes were associated with "complement and coagulation cascades" and "Th17 cell differentiation." These findings highlight the regulatory complexity of m^6A in modulating transcriptional responses during CVB3 infection and its potential role in orchestrating both immune and metabolic pathways.

We analyzed both in vivo and in vitro sequencing data and identified four genes—*Igtp, ApoI9b, Ddit3*, and *Irgm2*—that exhibited significant and consistent expression changes. qRT-PCR validation confirmed the RNA-seq findings for all genes, except for *ApoI9b*, in myocardial tissues from CVB3-infected mice. CVB3 infection notably upregulated the mRNA levels of *Igtp, Ddit3*, and *Irgm2* in both models. Igtp and Irgm2, key regulators of interferon (IFN) signaling, are part of the immune-related GTPase family, which plays a crucial role in resistance to intracellular pathogens.[40,41] Specifically, Igtp is involved in vesicular trafficking for pathogen clearance, while Irgm2 may regulate autophagy during innate immune responses.[42,43] Previous research has shown that Igtp can inhibit CVB3-induced apoptosis in cardiomyocytes by activating the PI3K/Akt signaling pathway.[44] However, the role of Irgm2 in CVB3-induced diseases remains unexplored. DDIT3 (also known as GADD153 or CHOP) is a transcription factor activated by stress, including ER stress, and regulates cell cycle arrest and apoptosis—processes central to many diseases.[45–47] Previous studies have established that CHOP upregulation due to ER stress contributes to CVB3-induced VMC by promoting cardiomyocyte apoptosis.[48] Additionally, IGV analysis demonstrated alterations in m^6A peak distributions in *Igtp, Ddit3*, and *Irgm2*, suggesting that m^6A modifications may participate in regulating their expression and functional responses to viral infection.

Additionally, we analyzed the expression of 36 m^6A regulators using RNA-seq data, followed by validation through qRT-PCR. Significant changes were observed in the expression of key regulators, including *IGF2BP2, EIF3H, RBM15B*, and *YTHDC2*. Among these regulators, IGF2BP2, EIF3H, and YTHDC2 function as m^6A readers, while RBM15B serves as an m^6A writer. IGF2BP2 is notably associated with signaling pathways such as PI3K/Akt,[49] TNF/NF-κB,[50,51] and FOXO.[52] EIF3H is linked to the Wnt[53] and Hippo signaling pathways,[54] whereas YTHDC2 participates in pathways including TNF,[55]

Akt,[56] NF-κB,[57] and Hippo.[58] Notably, previous studies have highlighted the close connection between CVB3 infection and these pathways. The PI3K/Akt signaling pathway, known for its roles in cell proliferation, apoptosis, and protein synthesis, is implicated in CVB3 infection.[59] Similarly, the MAPK signaling pathway is activated by CVB3, promoting inflammation, apoptosis, and viral replication in host cells.[35,60] The TNF signaling pathway contributes to inflammation, immune responses, and apoptosis, playing a pivotal role in creating an inflammatory environment and inducing cellular damage during CVB3 infection.[61,62] Furthermore, CVB3 has been shown to suppress the activation of NLRP3 inflammasomes by inhibiting the NF-κB signaling pathway, thereby enhancing host susceptibility to infection.[63] These findings suggest that m^6A regulators may play a critical role in modulating these signaling pathways during VMC.

Intriguingly, our analysis of in vivo and in vitro RNA-seq data on m^6A-related differential genes revealed that RBM15B exhibited the most significant upregulation, suggesting its potential as a key target in CVB3-induced VMC. RBM15B, a core component of the m6A methyltransferase complex, binds METTL3 and WTAP proteins to recruit them to specific RNA loci for site-specific methylation.[64] To explore its functional role, we demonstrated that RBM15B knockdown in HL-1 cells significantly attenuated both viral replication and apoptosis upon CVB3 infection. These findings highlight the pivotal involvement of m^6A regulators in modulating critical signaling pathways driving VMC progression. Notably, studies indicate that the m^6A methyltransferase complex deposits m^6A marks on nascent transcripts of promoter-associated RNAs and enhancer RNAs, thereby protecting their 5′ ends from endonuclease cleavage.[65] This implies that CVB3 infection may exploit RBM15B-mediated m^6A methylation to manipulate mRNA stability and translational efficiency, ultimately exacerbating cardiomyocyte apoptosis and viral replication. However, this mechanistic link requires further validation.

In summary, this study provides the first transcriptome-wide map of m^6A modifications in CVB3-induced VMC, revealing that m^6A serves as a dynamic regulator of gene expression and signaling networks in response to viral infection. These findings not only advance our understanding of CVB3 pathogenesis but also offer potential m^6A-related targets for therapeutic intervention. Nevertheless, further studies incorporating clinical samples are essential to validate these experimental observations and evaluate their translational relevance.

Data Sharing Statement

The datasets produced and/or analyzed in this study can be obtained from the corresponding author upon reasonable request.

Ethical Approval

All animal experiments were conducted in compliance with the ARRIVE guidelines (NC3Rs) and in accordance with the Guidelines for Ethical Review of Laboratory Animal Welfare (GB/T 35892-2018) issued by the Standardization Administration of China. The experimental protocols were reviewed and approved by the Ethics Committee of the Department of Laboratory Animals at Central South University (Approval No.2021sydw0104).

Funding

This study was funded by grants and support from the following organizations and foundations: National Natural Science Foundation of China (No. 81570346), Natural Science Foundation of Sichuan Province (No. 2025ZNSFSC1700) and Natural Science Foundation of Hunan Province (No. 2022JJ40739).

Disclosure

The authors report no conflicts of interest in this work.

References

1. Law YM, Lal AK, Chen S, et al. Diagnosis and Management of Myocarditis in Children: a Scientific Statement From the American Heart Association. *Circulation*. 2021;144(6):e123–e35. doi:10.1161/CIR.0000000000001001
2. Trachtenberg BH, Hare JM. Inflammatory Cardiomyopathic Syndromes. *Circ Res*. 2017;121(7):803–818. doi:10.1161/CIRCRESAHA.117.310221
3. Kwong JS. Herbal medicines for viral myocarditis. *Cochrane Database Syst Rev*. 2012;11:CD003711.
4. Tschope C, Ammirati E, Bozkurt B, et al. Myocarditis and inflammatory cardiomyopathy: current evidence and future directions. *Nat Rev Cardiol*. 2021;18(3):169–193. doi:10.1038/s41569-020-00435-x

5. Rohrbeck M, Hoerr V, Piccini I, et al. Pathophysiological Mechanisms of Cardiac Dysfunction in Transgenic Mice with Viral Myocarditis. *Cells*. 2023;13(1):12. doi:10.3390/cells13010012
6. Liu ZX, Li LM, Sun HL, Liu SM. Link Between m6A Modification and Cancers. *Front Bioeng Biotechnol*. 2018;6:89. doi:10.3389/fbioe.2018.00089
7. Jiang X, Liu B, Nie Z, et al. The role of m6A modification in the biological functions and diseases. *Signal Transduct Target Ther*. 2021;6(1):74. doi:10.1038/s41392-020-00450-x
8. Roignant JY, Soller M. m(6)A in mRNA: an Ancient Mechanism for Fine-Tuning Gene Expression. *Trends Genet*. 2017;33(6):380–390. doi:10.1016/j.tig.2017.04.003
9. Shi H, Zhang X, Weng YL, et al. m(6)A facilitates hippocampus-dependent learning and memory through YTHDF1. *Nature*. 2018;563(7730):249–253. doi:10.1038/s41586-018-0666-1
10. Fattahi S, Pilehchian Langroudi M, Akhavan-Niaki H. Hedgehog signaling pathway: epigenetic regulation and role in disease and cancer development. *J Cell Physiol*. 2018;233(8):5726–5735. doi:10.1002/jcp.26506
11. Fu Y, Dominissini D, Rechavi G, He C. Gene expression regulation mediated through reversible m(6)A RNA methylation. *Nat Rev Genet*. 2014;15(5):293–306. doi:10.1038/nrg3724
12. Dominissini D, Rechavi G. Epitranscriptome regulation. *Nat Struct Mol Biol*. 2018. doi:10.1038/s41594-018-0140-7
13. Roundtree IA, Evans ME, Pan T, He C. Dynamic RNA Modifications in Gene Expression Regulation. *Cell*. 2017;169(7):1187–1200. doi:10.1016/j.cell.2017.05.045
14. Song J, Yi C. Reading Chemical Modifications in the Transcriptome. *J Mol Biol*. 2020;432(6):1824–1839. doi:10.1016/j.jmb.2019.10.006
15. Frye M, Jaffrey SR, Pan T, Rechavi G, Suzuki T. RNA modifications: what have we learned and where are we headed? *Nat Rev Genet*. 2016;17(6):365–372. doi:10.1038/nrg.2016.47
16. Teng F, Tang W, Wuniqiemu T, et al. N(6)-Methyladenosine Methylomic Landscape of Lung Tissues in Murine Acute Allergic Asthma. *Front Immunol*. 2021;12:740571. doi:10.3389/fimmu.2021.740571
17. Guo M, Yan R, Ji Q, et al. IFN regulatory Factor-1 induced macrophage pyroptosis by modulating m6A modification of circ_0029589 in patients with acute coronary syndrome. *Int Immunopharmacol*. 2020;86:106800. doi:10.1016/j.intimp.2020.106800
18. Lu TX, Zheng Z, Zhang L, et al. A New Model of Spontaneous Colitis in Mice Induced by Deletion of an RNA m(6)A Methyltransferase Component METTL14 in T Cells. *Cell Mol Gastroenterol Hepatol*. 2020;10(4):747–761. doi:10.1016/j.jcmgh.2020.07.001
19. Kennedy EM, Bogerd HP, Kornepati AV, et al. Posttranscriptional m(6)A Editing of HIV-1 mRNAs Enhances Viral Gene Expression. *Cell Host Microbe*. 2016;19(5):675–685. doi:10.1016/j.chom.2016.04.002
20. Gokhale NS, McIntyre ABR, McFadden MJ, et al. N6-Methyladenosine in Flaviviridae Viral RNA Genomes Regulates Infection. *Cell Host Microbe*. 2016;20(5):654–665. doi:10.1016/j.chom.2016.09.015
21. Lichinchi G, Zhao BS, Wu Y, et al. Dynamics of Human and Viral RNA Methylation during Zika Virus Infection. *Cell Host Microbe*. 2016;20(5):666–673. doi:10.1016/j.chom.2016.10.002
22. Liu J, Xu YP, Li K, et al. The m(6)A methylome of SARS-CoV-2 in host cells. *Cell Res*. 2021;31(4):404–414. doi:10.1038/s41422-020-00465-7
23. Wang Y, Jia L, Shen J, et al. Cathepsin B aggravates coxsackievirus B3-induced myocarditis through activating the inflammasome and promoting pyroptosis. *PLoS Pathog*. 2018;14:e1006872.
24. Yang Y, Li W, You B, Zhou C. Advances in cell ^{death} mechanisms involved in viral myocarditis. *Front Cardiovasc Med*. 2022;9:968752. doi:10.3389/fcvm.2022.968752
25. Garmaroudi FS, Marchant D, Hendry R, et al. Coxsackievirus B3 replication and pathogenesis. *Future Microbiol*. 2015;10(4):629–653. doi:10.2217/fmb.15.5
26. Dimock K, Stoltzfus CM. Sequence specificity of internal methylation in B77 avian sarcoma virus RNA subunits. *Biochemistry*. 1977;16(3):471–478. doi:10.1021/bi00622a021
27. Kane SE, Beemon K. Precise localization of m6A in Rous sarcoma virus RNA reveals clustering of methylation sites: implications for RNA processing. *Mol Cell Biol*. 1985;5(9):2298–2306. doi:10.1128/mcb.5.9.2298-2306.1985
28. Lavi S, Shatkin AJ. Methylated simian virus 40-specific RNA from nuclei and cytoplasm of infected BSC-1 cells. *Proc Natl Acad Sci U S A*. 1975;72(6):2012–2016. doi:10.1073/pnas.72.6.2012
29. Huang H, Chen J, Chen J. The Biogenesis and Precise Control of RNA m(6)A Methylation. *Trends Genet*. 2020;36:44–52. doi:10.1016/j.tig.2019.10.011
30. Mayr C. What Are 3' UTRs Doing? *Cold Spring Harb Perspect Biol*. 2019;11:1.
31. Shim SH, Kim DS, Cho W, Nam JH. Coxsackievirus B3 regulates T-cell infiltration into the heart by lymphocyte function-associated antigen-1 activation via the cAMP/Rap1 axis. *J Gen Virol*. 2014;95(9):2010–2018. doi:10.1099/vir.0.065755-0
32. Xin L, Ma X, Xiao Z, Yao H, Liu Z. Coxsackievirus B3 induces autophagy in HeLa cells via the AMPK/MEK/ERK and Ras/Raf/MEK/ERK signaling pathways. *Infect Genet Evol*. 2015;36:46–54. doi:10.1016/j.meegid.2015.08.026
33. Liu T, Li Y, Chen S, et al. CircDDX17 enhances coxsackievirus B3 replication through regulating miR-1248/NOTCH receptor 2 axis. *Front Microbiol*. 2022;13:1012124. doi:10.3389/fmicb.2022.1012124
34. Li X, Zhang J, Chen Z, et al. Both PI3K- and mTOR-signaling pathways take part in CVB3-induced apoptosis of Hela cells. *DNA Cell Biol*. 2013;32(7):359–370. doi:10.1089/dna.2013.2003
35. He F, Xiao Z, Yao H, et al. The protective role of microRNA-21 against coxsackievirus B3 infection through targeting the MAP2K3/P38 MAPK signaling pathway. *J Transl Med*. 2019;17(1):335. doi:10.1186/s12967-019-2077-y
36. Meng Y, Sun T, Wu C, Xiong S, Xiong S. Calpain regulates CVB3 induced viral myocarditis by promoting autophagic flux upon infection. *Microbes Infect*. 2020;22(1):46–54. doi:10.1016/j.micinf.2019.07.001
37. Lv W, Li T, Li X, et al. Dynamic regulation and functions of mRNA m6A modification. *Cancer Cell Int*. 2022;22(1):48. doi:10.1186/s12935-022-02452-x
38. Feng H, Yuan X, Wu S, et al. Effects of writers, erasers and readers within miRNA-related m6A modification in cancers. *Cell Prolif*. 2023 56:e13340.
39. Hong J, Xu K, Lee JH. Biological roles of the RNA m(6)A modification and its implications in cancer. *Exp Mol Med*. 2022;54(11):1822–1832. doi:10.1038/s12276-022-00897-8
40. Henry SC, Daniell X, Indaram M, et al. Impaired Macrophage Function Underscores Susceptibility to Salmonella in Mice Lacking Irgm1 (LRG-47). *J Immunol*. 2007;179(10):6963–6972. doi:10.4049/jimmunol.179.10.6963

41. Hunn JP, Feng CG, Sher A, Howard JC. The immunity-related GTPases in mammals: a fast-evolving cell-autonomous resistance system against intracellular pathogens. *Mamm Genome*. 2011;22(1–2):43–54. doi:10.1007/s00335-010-9293-3
42. Taylor GA, Collazo CM, Yap GS, et al. Pathogen-specific loss of host resistance in mice lacking the IFN-gamma-inducible gene IGTP. *Proc Natl Acad Sci U S A*. 2000;97(2):751–755. doi:10.1073/pnas.97.2.751
43. Santiago HC, Feng CG, Bafica A, et al. Mice Deficient in LRG-47 Display Enhanced Susceptibility to Trypanosoma cruzi Infection Associated with Defective Hemopoiesis and Intracellular Control of Parasite Growth. *J Immunol*. 2005;175(12):8165–8172. doi:10.4049/jimmunol.175.12.8165
44. Zhang HM, Yuan J, Cheung P, et al. Overexpression of interferon-gamma-inducible GTPase inhibits coxsackievirus B3-induced apoptosis through the activation of the phosphatidylinositol 3-kinase/Akt pathway and inhibition of viral replication. *J Biol Chem*. 2003;278(35):33011–33019. doi:10.1074/jbc.M305352200
45. Xiang S, Gu H, Jin L, Thorne RF, Zhang XD, Wu M. LncRNA IDH1-AS1 links the functions of c-Myc and HIF1alpha via IDH1 to regulate the Warburg effect. *Proc Natl Acad Sci U S A*. 2018;115(7):E1465–E74. doi:10.1073/pnas.1711257115
46. Li M, Thorne RF, Shi R, et al. DDIT3 Directs a Dual Mechanism to Balance Glycolysis and Oxidative Phosphorylation during Glutamine Deprivation. *Adv Sci (Weinh)*. 2021;8(11):e2003732. doi:10.1002/advs.202003732
47. Diaz-Perez JA, Kerr DA. Gene of the month: DDIT3. *J Clin Pathol*. 2024;77(4):211–216. doi:10.1136/jcp-2023-208963
48. Cai Z, Shen L, Ma H, et al. Involvement of Endoplasmic Reticulum Stress-Mediated C/EBP Homologous Protein Activation in Coxsackievirus B3-Induced Acute Viral Myocarditis. *Circ Heart Fail*. 2015;8(4):809–818. doi:10.1161/CIRCHEARTFAILURE.114.001244
49. Liu X, He H, Zhang F, et al. m6A methylated EphA2 and VEGFA through IGF2BP2/3 regulation promotes vasculogenic mimicry in colorectal cancer via PI3K/AKT and ERK1/2 signaling. *Cell Death Dis*. 2022;13(5):483. doi:10.1038/s41419-022-04950-2
50. Bechara R, Amatya N, Bailey RD, et al. The m 6 A reader IMP2 directs autoimmune inflammation through an IL-17– and TNFα-dependent C/EBP transcription factor axis. *Sci Immunol*. 2021;6(61). doi:10.1126/sciimmunol.abd1287.
51. Lu Y, Qie D, Yang F, Wu J. LncRNA MEG3 aggravates adipocyte inflammation and insulin resistance by targeting IGF2BP2 to activate TLR4/NF-kappaB signaling pathway. *Int Immunopharmacol*. 2023;121:110467. doi:10.1016/j.intimp.2023.110467
52. Ye M, Chen J, Lu F, et al. Down-regulated FTO and ALKBH5 co-operatively activates FOXO signaling through m6A methylation modification in HK2 mRNA mediated by IGF2BP2 to enhance glycolysis in colorectal cancer. *Cell Biosci*. 2023;13(1):148. doi:10.1186/s13578-023-01100-9
53. Wei Y, Chen W, Li Z, Xie K, Liu F. EIF3H stabilizes CCND1 to promotes intrahepatic cholangiocarcinoma progression via Wnt/β-catenin signaling. *FASEB J*. 2022;36(12):e22647. doi:10.1096/fj.202200913R
54. Ponzoni L, Luo A, Zhu R, et al. EIF3H Orchestrates Hippo Pathway-Mediated Oncogenesis via Catalytic Control of YAP Stability. *Cancer Res*. 2020;80(12):2550–2563. doi:10.1158/0008-5472.CAN-19-3718
55. Tanabe A, Konno J, Tanikawa K, Sahara H. Transcriptional machinery of TNF-alpha-inducible YTH domain containing 2 (YTHDC2) gene. *Gene*. 2014;535(1):24–32. doi:10.1016/j.gene.2013.11.005
56. Zhou G, Wang S. YTHDC2 Retards Cell Proliferation and Triggers Apoptosis in Papillary Thyroid Cancer by Regulating CYLD-Mediated Inactivation of Akt Signaling. *Appl Biochem Biotechnol*. 2024;196(1):588–603. doi:10.1007/s12010-023-04540-8
57. Wang J, Tan L, Jia B, et al. Downregulation of m 6 A Reader YTHDC2 Promotes the Proliferation and Migration of Malignant Lung Cells via CYLD/NF-κB Pathway. *Int J Biol Sci*. 2021;17(10):2633–2651. doi:10.7150/ijbs.58514
58. Zhou X, Chang L, Liang Q, et al. The m6A methyltransferase METTL3 drives thyroid cancer progression and lymph node metastasis by targeting LINC00894. *Cancer Cell Int*. 2024;24(1):47. doi:10.1186/s12935-024-03240-5
59. Wei J, Wang DF, Cui CC, Tan JJ, Peng MY, Lu HX. CXCL4/CXCR3 axis regulates cardiac fibrosis by activating TGF-beta1/Smad2/3 signaling in mouse viral myocarditis. *Immun Inflamm Dis*. 2024;12(4):e1237. doi:10.1002/iid3.1237
60. Si X, Luo H, Morgan A, et al. Stress-activated protein kinases are involved in coxsackievirus B3 viral progeny release. *J Virol*. 2005;79(22):13875–13881. doi:10.1128/JVI.79.22.13875-13881.2005
61. Fairweather D, Frisancho-Kiss S, Yusung SA, et al. IL-12 protects against coxsackievirus B3-induced myocarditis by increasing IFN-gamma and macrophage and neutrophil populations in the heart. *J Immunol*. 2005;174(1):261–269. doi:10.4049/jimmunol.174.1.261
62. Zhou J, Li P, Sun S, et al. Necroptosis and Viral Myocarditis: tumor Necrosis Factor alpha as a Novel Biomarker for the Diagnosis of Viral Myocarditis. *Front Cell Dev Biol*. 2022;10:826904. doi:10.3389/fcell.2022.826904
63. Sun Z, Zhang H, Xu W, et al. CVB3 Inhibits NLRP3 Inflammasome Activation by Suppressing NF-kappaB Pathway and ROS Production in LPS-Induced Macrophages. *Viruses*. 2023;15:1.
64. Patil DP, Chen CK, Pickering BF, et al. m(6)A RNA methylation promotes XIST-mediated transcriptional repression. *Nature*. 2016;537(7620):369–373. doi:10.1038/nature19342
65. Xu W, He C, Kaye EG, et al. Dynamic control of chromatin-associated m(6)A methylation regulates nascent RNA synthesis. *Mol Cell*. 2022;82(6):1156–68e7. doi:10.1016/j.molcel.2022.02.006